ICPMG 2026

Proceedings of the 11th ICPMG 2026
11th International Conference on Physical Modelling in Geotechnics
8-12 June 2026, Zurich, Switzerland

Advancing Physical Modeling with Aluminum Rod Model Ground： Confining Pressure Effects on Deformation Characteristics

Y. Egoshi
Graduate School of Science and Engineering/Chuo University, Tokyo, Japan, a21.rf3a@g.chuo-u.ac.jp

M. Yagawa, H. Nishioka
Graduate School of Science and Engineering/Chuo University, Tokyo, Japan, a21.wr8x@g.chuo-u.ac.jp, nishioka@civil.chuo-u.ac.jp

ABSTRACT: Studies investigating the effects of soil–structure interactions on foundations and underground structures often conduct model ground tests using aluminum rod assemblies. This arrangement reproduces the characteristics of granular materials, ensures two-dimensional conditions, provides intuitive visualization, and enables straightforward evaluation through image analysis.
To accurately evaluate results and apply them to the understanding of actual ground behavior, it is necessary to further elucidate the inherent properties of the aluminum-rod model ground. Although properties such as the internal friction angle and dilatancy have previously been investigated, detailed deformation characteristics—particularly the confining pressure dependency and strain-level dependency of the deformation modulus—remain insufficiently understood.
Therefore, this study aimed to clarify these deformation characteristics of the aluminum-rod model ground by conducting plane strain compression tests, a physical modeling method corresponding to laboratory tests on sand. The aluminium-rod specimens measuring 200 × 200 mm were prepared by stacking aluminum rods of different diameters. While maintaining the confining pressure exerted by the side walls at a constant value, the top plate was lowered to increase vertical stress. The vertical stress and displacements of the side walls and top plate were then measured, focusing on the effect of confining pressure on the deformation characteristics of the aluminum-rod model ground. The secantmodulus exhibited an approximately first-order dependence on confining pressure, indicating higher sensitivity to confining pressure than that of sand(three-dimensional granular materials).

1 RESEARCH BACKGROUND

Studies investigating the effects of soil–structure interactions on foundations and underground structures often conduct model ground tests using aluminum rods masses (Matsuoka, 1974; Ukai, 1992; Nakai et al., 1999; Shahin et al., 2004; Chao et al., 2020; Sasaki et al., 2022; Yosida et al., 2023; Sagawa et al., 2024; Hirano et al., 2024; Yagawa et al., 2025;）. This arrangement reproduces the characteristics of granular materials, ensures two-dimensional conditions, provides intuitive visualization, and enables straightforward evaluation through image analysis.
The authors haves previously conducted model tests using this aluminium-rod ground, such as the example shown in Figure 1, to investigate the confining pressure dependency of the coefficient of subgrade reaction for deeply embedded column-type foundations similar to those used in large bridge

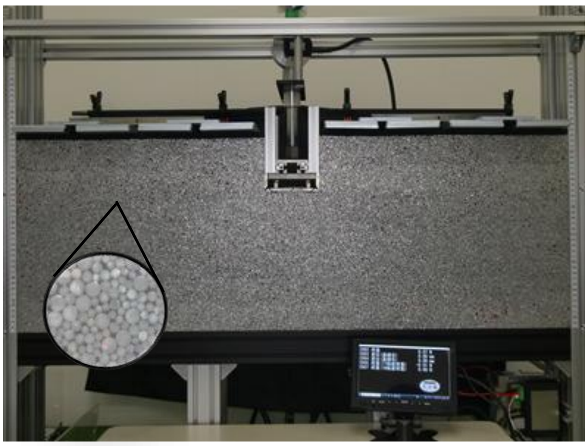

Figure 1. Model experiments on the bearing capacity of foundations(Egoshi et al, 2024)

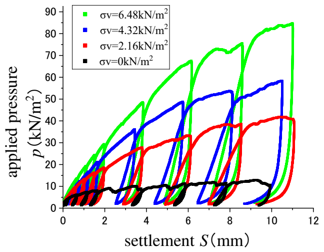

Figure 2. A example of the model experiments results for foundations(Egoshi et al, 2024)

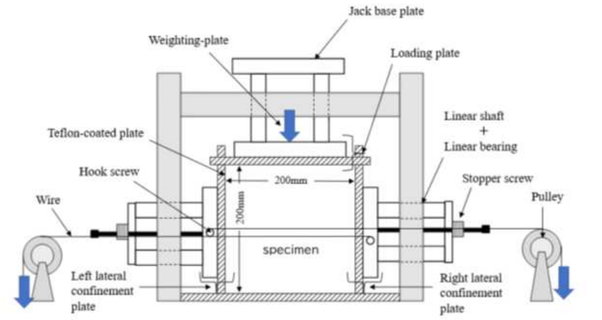

Figure 3. Front view of the plane strain compression testing apparatus

structures. As an example of the experimental results obtained under different confining pressures, Figure 2 shows the relationships between applied pressure and settlement (left), and between the coefficient of subgrade reaction and settlement (right). Accurate evaluation of the coefficient of subgrade reaction is essential for predicting settlement during construction. However, due to limitations of the loading apparatus in the model tests, the overburden pressure that would actually act on the foundation in the field is not properly applied during the evaluation process. Consequently, it is necessary to correct the obtained coefficient of subgrade reaction to account for the influence of overburden pressure, yet no established method for such correction has been proposed.

In a previous study, Inohara et al. (2017) suggested that the confining pressure dependency of the coefficient of subgrade reaction could potentially be estimated from the confining pressure dependency of the deformation modulus obtained through triaxial compression tests. However, their study was based on experiments conducted using an actual caisson foundation during the sinking process, and the results were limited in scope and reproducibility. It therefore remains unclear whether, in model experiments, the confining pressure dependency of the coefficient of subgrade reaction originates from the intrinsic confining pressure dependency of the material at the particle-assembly level.

Regarding the material properties of aluminium-rod assemblies used in model tests, fundamental mechanical characteristics have been clarified through biaxial tests conducted by Matsuoka et al. (1994), and biaxial tests under varying confining pressures have been performed by Sukhumkitcharoen et al. (2023) Nevertheless, no study has specifically focused on the confining pressure dependency of the deformation modulus. Clarifying this issue is considered essential not only for understanding the detailed behavior of aluminium-rod model ground but also for rational interpretation of model test results. While previous studies on aluminum-rod specimens (Matsuoka et al., 1994; Sukhumkitcharoen et al., 2023) have primarily utilized the term 'biaxial tests', this study adopts the term 'plane strain compression tests' to align with the physical modeling of actual laboratory tests on sand. In this approach, the mean principal stress is calculated by accounting for the intermediate principal stress, mirroring the evaluation methods used in plane strain compression tests. This framework is intended to facilitate future discussions regarding the correspondence between experimental results and two-dimensional plane strain conditions in numerical analyses.

Therefore, in the present study, plane strain compression tests were conducted on specimens composed of mixed-diameter aluminum rods in order to explicitly identify the confining pressure dependency at the material level.

In these tests, the horizontal stress σ_h was maintained constant while the vertical stress σ_v was increased. The confining pressure dependency of the deformation modulus was evaluated at different strain levels using power-law relationships, and the results were further compared with known deformation characteristics of sand.

2 EXPERIMENT

2.1 Overview of the testing apparatus

Figure 3 presents a front-view schematic of the plane strain compression testing apparatus used in this study, and Figure 4 shows an overall view of the apparatus. The main features of the apparatus are summarized as follows.

1) The specimen consisted of an aluminum-rod assembly measuring 200 mm × 200 mm with a depth of 150 mm.

2) The loading plate on the top and the lateral confinement plates are movable. Each plate can translate vertically or horizontally without tilting, as its motion is guided by two linear shafts and linear bearings. Two strip-shaped plates are attached to the loading plate, and three are attached to each lateral side. At the corner sections, these plates interlock in a f20inger-joint–like configuration, allowing them to

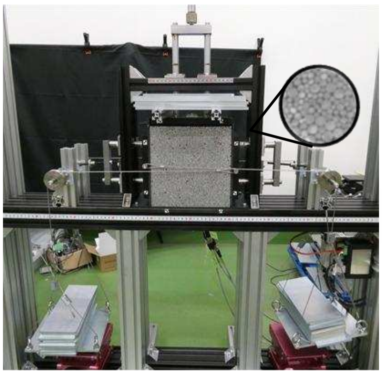

Figure 4. Overall view of the testing apparatus

Figure 5. Structure of the corner section

follow the specimen deformation (Figure 5). In addition, the plate surfaces are coated with fluoropolymer to reduce friction against the aluminum rods.

3) The loading plate is driven downward by an electrically actuated jack installed above the specimen, which operates under displacement control. However, the initial vertical stress σ_{v0} is not applied by the jack; instead, it is generated by the self-weight of the loading plate and an additional weighting plate placed between the jack and the loading plate. The incremental vertical load applied by the jack is measured using a load cell directly connected to the jack. The vertical stress σ_v is calculated by dividing the vertical load by the initial top-surface area of the specimen.

4) The lateral confinement plates compress the specimen from both sides through the tension applied to the wires. Specifically, the wire attached to the left confinement plate passes along the front and back of the aluminum-rod assembly, runs over a pulley on the right side, and connects to a weighting plate. Through this mechanism, the lateral confinement plates apply a constant horizontal stress σ_{h0} to the specimen during testing, effectively clamping it from both sides. During specimen preparation, the confinement plates are fixed in place using stopper screws. The horizontal stress σ_{h0} is calculated by dividing the weight of the weighting plate attached to the end of each wire by the initial lateral surface area of the specimen; in this calculation, the resistances of the linear bearings and pulleys are neglected.

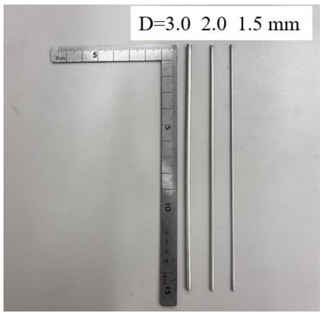

Figure 6. Aluminum rods used

Table 1. Experimental Case

	Initial Stress σ_{vo}=σ_{h0} (kN/m^2)	Unit Weight (kN/m^3)
Case1	4.98	21.6
Case2	9.00	21.5
Case3	13.6	21.6

5) The displacements of the loading plate and the left and right lateral confinement plates are measured by attaching target plates to each plate and monitoring them with laser displacement sensors. In addition, photographs of the specimen are taken during testing for image-based analysis. The spatial resolution of the captured images is approximately 0.1 mm per pixel.

2.2 Specimen

The aluminium-rod specimen was composed of mixed diameter aluminum rods with a length of 150 mm and diameters of 1.5 mm, 2 mm, and 3 mm (Figure 6), mixed at a weight ratio of 1:1:1. The aluminum rods are cylindrical with approximately circular cross-sections; however, slight deformation is observed in some rods. The angle at which rolling initiates is approximately 2–3 degrees. The movable lateral confinement plates were fixed at a width of 200 mm, and the aluminum rods were placed in 50 mm thick layers. Each layer was compacted using a small vibrator and stacked until a total height of 200 mm was achieved. The unit weight of the aluminum-rod specimen in this study ranged from 21.5 to 21.6 kN/m³ (Table 1). To characterize the density of these specimens, the values were compared with those reported by Nishioka et al. (2022), who used mixed-diameter aluminum rods with the same particle shape and particle size distribution. In the study by Nishioka et al., the average unit weight for 'loose' ground—prepared by simply aligning the rods without any compaction—was 21.18 kN/m³, while that for 'dense' ground— achieved by thoroughly compacting the rods with a vibrator—was 21.85 kN/m³. Since the unit weights obtained in this study fall between these two benchmarks, the aluminum-rod specimen condition can be classified as medium dense.

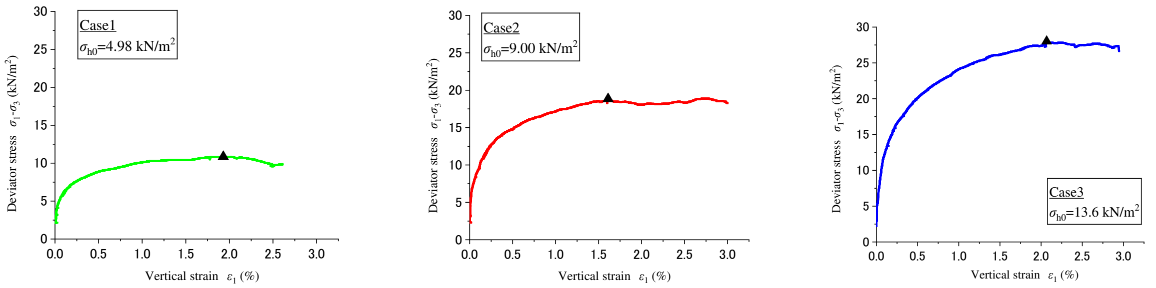

Figure 7. Relationship between Deviator stress σ_1-σ_3 -Vertical strain ε_1

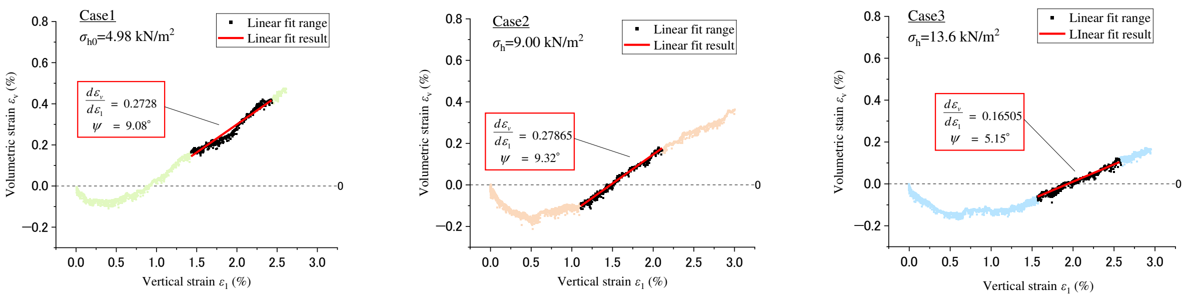

Figure 8. Relationship between Volumetric strain ε_v -Vertical strain ε_1

2.3 Initial Stress and Test Cases

In this study, the initial stress state prior to loading was set to an isotropic condition in which the initial vertical stress σ_{v0} and the horizontal stress σ_{h0} were equal. Using this initial stress as an experimental parameter, three test cases (referred to as Case 1, Case 2, and Case 3) were conducted with σ_{h0}= 4.98, 9.00, and 13.6 kPa, respectively. It was confirmed that repeated tests conducted under the same case conditions yielded consistent results, provided that the specimens had comparable densities. Table 1 summarizes the initial stresses and unit weight of the specimen under the initial conditions.

After establishing the initial stress state, vertical loading was applied using the displacement-controlled jack. The loading rate was initially set to 0.01 mm/s up to a vertical displacement of 4 mm (corresponding to 2% vertical strain), and then increased to 0.02 mm/s thereafter.

3 EXPERIIMENTAL RESULTS

3.1 Stress-Strain Relationship and Dilatancy

The deviator stress σ_1-σ_3 –axial strain ε_1 relationships for each test case are presented in Figure 7. The vertical stress within the specimen is non-uniform, increasing with depth due to self-weight, and the difference between the top and bottom is approximately 4 kPa. Although the horizontal stress is likewise expected to increase with depth, the following discussion assumes that a uniform vertical stress corresponding to the specimen mid-height acts over the entire specimen. The results are summarized using representative values of the principal stresses, σ_1 and σ_3, for the specimen as a whole. As shown in the figure, the maximum deviator stress increases with increasing horizontal stress σ_{h0}, and in all cases the peak value is reached at an axial strain of approximately 1-2%. In addition, little post-peak stress reduction is observed.

The volumetric strain ε_v – axial strain ε_1 relationships for each test case are presented in Figure 8. As shown in the figure, all cases exhibit a small amount of volumetric contraction at the initial stage of loading, indicated by negative volumetric strain, with the minimum value occurring at an axial strain of approximately 0.5-1.0%. Thereafter, the volumetric strain reverses its trend and begins to increase. Once the axial strain exceeds approximately 0.5-1.0%, the volumetric strain becomes positive, indicating volumetric expansion and the development of positive dilatancy. In addition, the magnitude of volumetric strain varies with confining pressure, and it is observed that higher horizontal stress σ_{h0} results in smaller volumetric strain.

Next, the dilatancy angle ψ was evaluated. As shown in Figure 8, a linear fitting was performed for the range within ±0.5% around the stress peak value identified in Figure 7 (indicated by the black region), and the fitted line is shown by the red line.

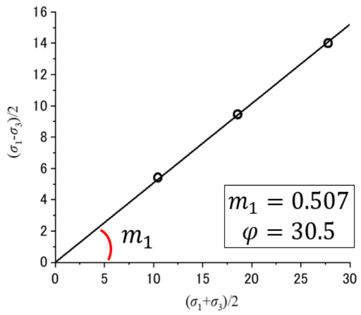

Figure 9. Determination of the Internal Friction Angle

The slope of this red line, $d\varepsilon_v/d\varepsilon_1$, was substituted into Equation (1) (Bolton, 1986; Schanz et al., 1996) to determine the dilatancy angle. As a result, the dilatancy angle ψ was approximately 9° for Cases 1 and 2, and approximately 5° for Case 3.

$$\psi = \arcsin\left\{\left(\frac{d\varepsilon_v}{d\varepsilon_1}\right) / \left(2 - \frac{d\varepsilon_v}{d\varepsilon_1}\right)\right\} \qquad (1)$$

3.2 Strength Characteristics

The strength characteristics were evaluated based on the stress state at failure. The internal friction angle was determined in accordance with the JSCE (2020) standard. For each test, the mean principal stress p and one-half of the deviator stress at the point where the deviator stress reached its maximum were plotted, and a linear regression was performed using the least-squares method (Figure 9). As the aluminum rods exhibit no cohesion and can be regarded as a φ-material, the regression line was constrained to pass through the origin. The slope m_1 of this fitted line was then substituted into Equation (2) to compute the internal friction angle, which was found to be approximately 30.5°.

$$\varphi = \sin^{-1} m_1 \qquad (2)$$

3.3 Validation of Strain Measurement Accuracy Using Image Analysis

In this experiment, displacement measurements obtained using laser displacement sensors were taken not from the specimen itself but from the displacements of the external lateral confinement plates and loading plate. Strain was calculated using these values. Therefore, particularly at small strain levels, bedding error may have occurred. To examine this potential error, Case 2 was analysed by measuring the internal displacement of the specimen using image analysis, and the resulting strain measurements were compared with those obtained from the external displacement measurements.

In this study, image analysis was conducted using Dip-Motion, a software package based on the Digital Image Correlation (DIC) method.

Figure 10 shows the tracked marker positions identified in the image analysis and a portion of the tracking results. The images used for the analysis were captured during the experiment at 3-second intervals using a digital camera. The image resolution was 5184 × 3888 pixels, corresponding to approximately 0.1 mm per pixel. The tracking markers were placed approximately 7 mm inward from each edge, with five markers assigned along each side. The displacement of each marker was obtained by performing pattern matching within a window of 7mm × 7 mm centered on the marker.

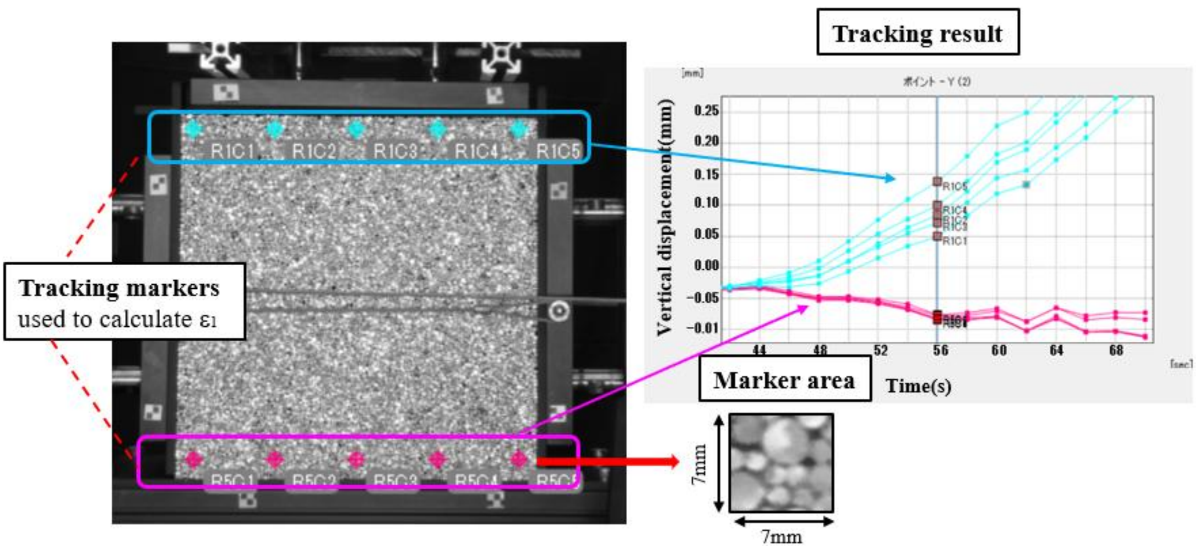

Figure 10. Trajectories of tracking markers in image analysis

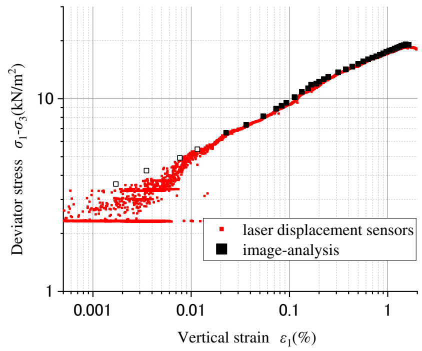

Figure 11. Comparison with Image analysis Results

The vertical strain ε_1 was calculated from the difference between the average vertical positions of the five markers along the top and bottom edges of the specimen. While it is generally recognized that the DIC method provides sub-pixel accuracy (Ueno et al., 2014), this analysis considered only the range in which the displacement exceeded one pixel (approximately 0.1 mm) to ensure a more robust and reliable level of measurement accuracy. Within this range, the corresponding vertical strain ε_1 and the vertical stress at each step were obtained. The vertical stress was determined from the jack load displayed on the monitor captured within the images.

Figure 11 presents the deviator stress–axial strain relationship for Case2 obtained from the laser displacement sensors (red line) in a log–log plot, on which the axial strains derived from the image-analysis-based displacements are superimposed as black dots. It is observed that, for $\varepsilon_1 \gtrsim 0.02\%$, results of image analysis and laser-based measurements show generally good agreement. The data plotted with open symbols for axial strains below 0.01% were judged to be unreliable and were excluded from further discussion, as fluctuations of the laser displacement sensors were relatively large in this strain range. A similar trend was confirmed from the independently evaluated relationship between horizontal strain ε_3 and vertical strain ε_1.

Based on these results, it is concluded that, in this experiment, the strain measurements obtained from the laser displacement sensors exhibit sufficient accuracy for vertical strains $\varepsilon_1 \geq 0.02\%$.

3.4 Strain-Level Dependence of Deformation Characteristics

In this study, the specimen is modeled as an equivalent linear elastic material within the range where the deviator stress has not yet reached its peak and where sufficient strain measurement accuracy is ensured by the laser displacement sensors, i.e., for vertical strains $\varepsilon_1 \geq 0.05\%$. The deformation

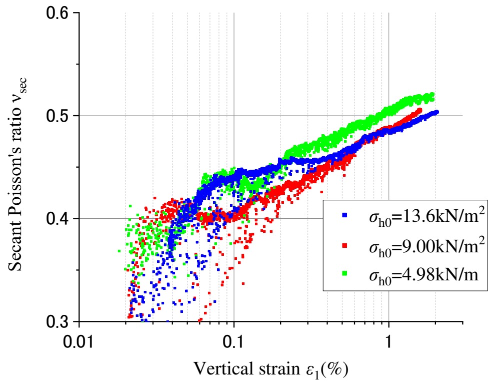

Figure 12. Secant Poisson's ratio ν_{sec}

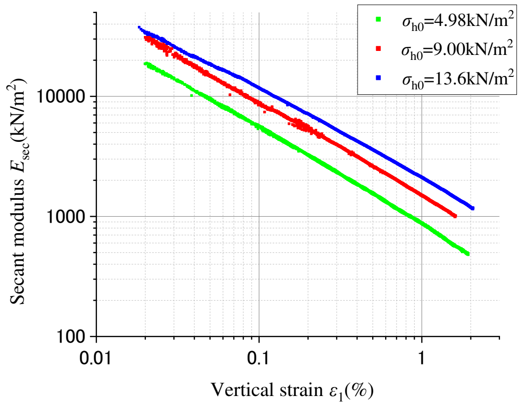

Figure 13 Secant Modulus E_{sec}–Verticall Strain ε_1 Relationship

characteristics, expressed in terms of the secant modulus E_{sec} and secant Poisson's ratio ν_{sec}, are evaluated within this strain range.

Because the aluminium-rod specimen represents a two-dimensional model simulating plane-strain conditions, it satisfies the elastic constitutive equations for plane strain, as given in Equations (3) and (4).

$$\varepsilon_1 = \frac{1}{E_{sec}}\left\{\left(1-\nu_{sec}{}^2\right)\sigma_1 - \nu\left(1+\nu_{sec}\right)\sigma_3\right\} \qquad (3)$$

$$\varepsilon_3 = \frac{1}{E_{sec}}\left\{\left(1-\nu_{sec}{}^2\right)\sigma_3 - \nu\left(1+\nu_{sec}\right)\sigma_1\right\} \qquad (4)$$

First, to verify the secant Poisson's ratio ν_{sec}, secant modulus E_{sec} is eliminated from Equations (3) and (4), yielding Equation (5).

$$\nu_{sec} = \frac{\varepsilon_1\sigma_3 - \varepsilon_3\sigma_1}{\left(\sigma_3+\sigma_1\right)\left(\varepsilon_1-\varepsilon_3\right)} \qquad (5)$$

Figure 12 shows the secant Poisson's ratio ν_{sec} back-calculated using Equation (4) from the measured

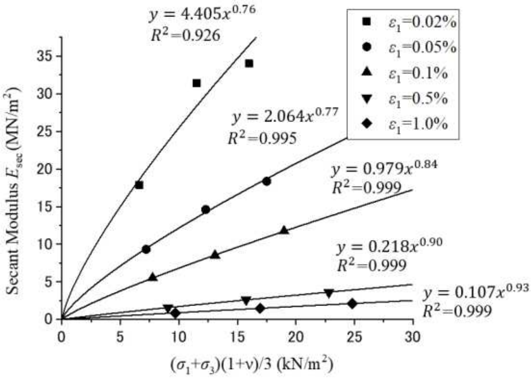

Figure 14. Confining pressure dependence Secant of Modulus E_{sec}

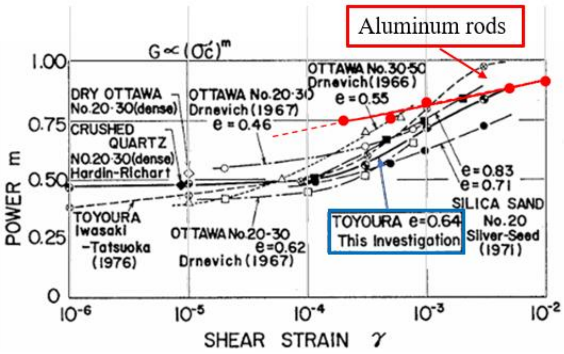

Figure 15. Comparison of Confining Pressure Dependency:Toyoura Sand and AluminumRods (modified from Kokusho, 1980)

vertical stress σ_1, horizontal stress σ_3, vertical strain ε_1, and horizontal strain ε_3 for each test case. Although some scatter is observed among the cases, the secant Poisson's ratio ν_{sec} of the aluminium-rod specimen is approximately 0.4 in the early stage of loading and gradually reaches 0.5 as failure approaches.

Next, the secant modulus E_{sec} during loading can be obtained from Equation (6), which is derived by rearranging Equation (3).

$$E_{sec} = \frac{\left\{\left(1-{\nu_{sec}}^2\right)\sigma_1 - \nu\left(1+\nu_{sec}\right)\sigma_3\right\}}{\varepsilon_1} \qquad (6)$$

In the following analysis, secant Poisson's ratio ν_{sec} was taken as an average value of 0.45 during loading, based on the results shown in Figure 12, and the modulus E_{sec} was back-calculated accordingly. Although, we must use the value obtained from Equation (5) at each strain level, it was confirmed separately that the resulting error is relatively small.

Figure 13 shows the relationship between E and axial strain. The deformation modulus exhibits an approximately linear trend on a log–log scale, indicating a clear dependence on the strain level.

3.5 Confining-Pressure Dependence of the Deformation Modulus

This section summarizes the influence of confining pressure on the test results. The deformation characteristics obtained under each confining pressure condition were compared to clarify the pressure dependency.

In Figure 14, the deformation moduli corresponding to axial strains of 0.02%, 0.05%, 0.1%, 0.5%, and 1% (all below the peak) were derived from power-law approximations over the strain range from 0.02% to the yield strain and plotted against the mean principal stress. Power-law relationships were then established for each strain level. The exponent of the power-law equations was found to start at approximately 0.76 and approach 0.93 as the stress level approached the peak.

Next, the confining pressure dependency of sand is considered for comparison. Kokusho (1980) summarised the dependency of the confining pressure on the shear modulus for various sands, reporting that the dependence exponent for sand is approximately 0.75 - 1.0 around a strain level of 0.5%, but decreases as the strain level becomes smaller, asymptotically approaching approximately 0.5 at around 0.01% or less. In Figure 15, the present results are plotted in red together with the results reported by Kokusho. For the aluminum-rod assembly, the power-law exponent representing the confining pressure dependency is comparable to that of sand at relatively large strain levels (greater than approximately 0.1%). However, at strain levels below 0.1%, the exponent is slightly higher than that of sand.

Although the very small strain range could not be measured in the present study, the slope of the exponent m with respect to strain is more gradual than that for sand. This suggests that even in the very small strain range, the exponent m may be larger than the commonly reported value of 0.5 for sand. The authors consider that this difference may be attributable to the difference in particle kinematics, namely, two-dimensional motion in the aluminum rod assembly versus three-dimensional motion in sand. This issue will be further examined through numerical analyses in future work.

Furthermore, in the authors' previous study on the coefficient of subgrade reaction for foundations (Figure 2), an increasing trend of the coefficient of subgrade reaction with confining pressure was observed. The deformation characteristics obtained in the present study are considered to provide fundamental data necessary for quantitatively comparing those results. However, in Figure 2, the mean principal stress is approximately twice that applied in the present tests. Therefore, whether the same tendency can be observed under higher confining pressure conditions remains to be examined in future studies.

4 CONCLUSIONS

In this study, plane strain compression tests were conducted to clarify the detailed deformation characteristics of aluminium-rod model ground, with the aim of examining the relationship between the confining pressure dependency of the coefficient of subgrade reaction and that of the deformation modulus, as well as its implications for similarity laws in model tests. The main findings are summarized as follows:

1. A distinct peak was observed in the stress–strain relationship, and the maximum principal stress difference increased with increasing confining pressure.
2. The initial loading caused volumetric contraction, followed by dilation, and the magnitude of dilatancy decreased with higher confining pressures.
3. The secant Poisson's ratio gradually increased from 0.4 at the initial loading stage to 0.5 at failure.
4. The exponent representing the confining pressure dependency increased gradually with strain level, ranging from 0.76 at 0.02% strain to 0.93 at 1% strain. At relatively large strain levels around 1%, the exponent was comparable to that of sand. In contrast, at intermediate strain levels between 0.02% and 0.1%, the exponent was found to be higher than that of sand.

REFERENCES

Bolton. M. D. (1986). The strength and dilatancy of sands. *Geotechnique* 36, No. I, 65-78. https://doi.org/10.1680/geot.1986.36.1.65

Egoshi, Y., Shikakura, R., Nishioka, H., Kurachi, S., Oshida, S., Okahisa, T. (2024). Confining Pressure Dependence of the Coefficient of Subgrade Reaction under Cyclic Loading. *Proceeding of 80th Annual Conference of the JSCE.* (in Japanese)

Hirano, M., Sasaki, Y., and Nishioka, H. (2024). Evaluation of the bearing capacity of scoured bridge foundations using aluminum rod ground model tests. *Natural Geo-Disasters and Resiliency. IC-CREST 2023. Lecture Notes in Civil Engineering*, Vol. 445, pp. 163-172. Springer, Singapore. http://doi.org/10.1007/978-981-99-9223-2_14

Inohara, T.,Uthumi, K., Kotake, T., (2017), Correction of subgrade reaction coefficient for overburden pressure based on plate loading tests inside a caisson. *Kisoko* ,pp.44-47.(in Japanese)

Japan Society of Civil Engineers (JSCE). (2020). Methods and commentary for testing of geotechnical materials, Vol. 2, pp. 594. Tokyo, Japan: JSCE. (in Japanese)

Kokusho, T. (1980). Cyclic triaxial test of dynamic *soil properties for wide strain range. Soils and Foundations*, Vol.20, No.2, pp 45–60. http://doi.org/10.3208/sandf1972.20.2_45

Matuoka, H. (1974). A microscopic study on shear mechanism of granular materials. *Soils and Foundations*, Vol.14, No.1, pp. 29–43. http://doi.org/10.3208/sandf1972.14.29

Matuoka, H., Yamamoto, S., (1994), A microscopic study on shear mechanism of granular materials by DEM. *Soils and Foundations,* No.487, pp.167-175. https://doi.org/10.2208/jscej.1994.487_167

Nishioka, H., Mathumoto, N., Fukuda, F., Ono, K., (2022). Model excavation tests simulating the collapse of high bending rigidity cantilever-type earth retaining walls and proposal of a simple calculating method for the reasonable embedding length. *Journal of Geotechnical and Geoenvironmental Engineering*, Vol.17, No.3, pp.401-420. (in Japanese) https://doi.org/10.3208/jgs.17.401

Sagawa, T., Ohata, T., and Nishioka, H. (2024). 2D model tests of sheet pile reinforcement method for existing pile foundations. *Climate Change Adaptation from Geotechnical Perspectives. CREST 2023. Lecture Notes in Civil Engineering*, Vol.447. Springer, Singapore. http://doi.org/10.1007/978-981-99-9215-7_10

Sasaki, Y., and Nishioka, H. (2022). Vertical loading tests on local scoured spread foundation on aluminum rods model ground. *GEOMATE Journal*, Vol.23, No.98, pp.17–23. https://geomatejournal.com/geomate/article/view/1472

Schanz T, Vermeer PA: Angles of friction and dilatancy of sand, *Geotechnique*, Vol. 46, No. 1, pp. 145-151, 1996. https://doi.org/10.1680/geot.1996.46.1.145

Sukhumkitcharoen, R., Koseki, J., Kyokawa, H., Otsubo, M. (2023). Liquefaction behaviour of aluminium and plastic rod assemblies using bi-axial apparatus with application of image analysis. *8th International Symposium on Deformation Characteristics of Geomaterials.*

Ueno, K., Sreng, S., and Kobayashi, K. (2014), Surface Kinematometry by image processing for geotechnical model test. *Proceedings of 8th international conference on physical modelling in geotechnics*. Vol.1, pp.337-343

Xu, C., Liang, C., Shen, P., and Chai, F. (2020). Experimental and numerical studies on the reinforcing mechanisms of geosynthetic-reinforced granular soil under a plane strain condition. *Soils and Foundations*, Vol.60, No.2, pp. 466–477. http://doi.org/10.1016/j.sandf.2020.03.003

Yagawa, M., Nishioka, H., Konishi, S., and Sakata, S. (2025). Aluminum rod model ground test used to determine vertical displacement of tunnel in longitudinal direction due to ground heave. *Proceedings of the 5th AsRTC6 Urban GeoEngineering Symposium*.